Chemical Science

Accepted Manuscript

This article can be cited before page numbers have been issued, to do this please use: H. Zhong, S. Chang, X. Zhou, A. Gao, Y. Luo, Y. L. Shan, L. Zhang, Z. Gui, X. Huang, X. Hu, T. Huo and L. Liu, *Chem. Sci.*, 2025, DOI: 10.1039/D5SC02632F.

ROYAL SOCIETY OF CHEMISTRY

rsc.li/chemical-science

View Article Online
DOI: 10.1039/D5SC02632F

Mass spectrometric Imaging of Organic and Metallic Metabolites by Plasmon-Induced Interfacial Charge-Transfer Transition (PICTT) on Au Sputtered ITO Slides

Shao Chang[1a, 1b‡], Xin Zhou[1c, 1d‡], Anji Gao[2a, 2b†‡], Yixiang Luo[1c, 1d], Yujia Shan[3a], Lin Zhang[4], Zhengwei Gui[4], Xingchen Huang[1a, 1b], Xiaoyuan Hu[1c, 1d], Tianci Huo[1c, 1d], Linhui Liu[3b] and Hongying Zhong[1a, 1b, 1c, 1d, 1e*]

[1]State Key Laboratory of Featured Metal Materials and Life-cycle Safety for Composite Structures[a], College of Life Science and Technology[b], Medical College of Guangxi University[c], Center for Instrumental Analysis[e], Guangxi University, Nanning, Guangxi 530004, P. R. China

[2] Innovation Academy for Precision Measurement Science and Technology[a], Chinese Academy of Science, Wuhan 430071, P. R. China. University of Chinese Academy of Science[b], Beijing 100049, P. R. China.

[3] School of Computer Science[a], National Key Laboratory of Green Pesticide, International Joint Research Center for Intelligent Biosensor Technology and Health, College of Chemistry[b], Central China Normal University, Wuhan, Hubei 430079, P. R. China.

[4] Tongji Medical College, Huazhong University of Science and Technology, Wuhan, Hubei 430030, P. R. China

‡These authors contribute equally.

†Visiting student of Guangxi University.

*Correspondence should be addressed. Email: hyzhong@gxu.edu.cn

View Article Online
DOI: 10.1039/D5SC02632F

Abstract

Protonation/deprotonation is the major ionization mechanism of organic molecules in current electrospray ionization (ESI) and matrix assisted laser desorption ionization mass spectrometric (MALDI MS) imaging. But cellular complexities are far beyond protonated or deprotonated organic molecules. There are tremendous endogenous organic and metallic metabolites that regulate oxidization-reduction homeostasis cannot be protonated or deprotonated. We describe an electron-driven ionization paradigm for mass spectrometric imaging of organic and metallic metabolites based on the charge and energy flow at the plasmonic metal-molecule interface. Enhanced plasmonic electron transfer was observed on Au sputtered ITO glass slides that were made with a physical vapor deposition approach. Plasmon-induced interfacial charge-transfer transition (PICTT) enables the decay of plasmons by direct excitation of electrons from Au atoms to strongly coupled electron receptors in tissues sections that are blotted on Au sputtered ITO slides. The highly reactive plasmonic hot electrons facilitates not only the mass spectrometric imaging of endogenous organic metabolites, but also the *in-situ* surface plasmon-driven chemical reactions that can generate coordinative species for the visualization of endogenous metal ions. Beyond the biological application, the PICTT MS technique provides a way to tackle with the nature of the electronic excitations at the plasmon–molecule interface that has been challenging because of the lack of suitable experimental tool to directly monitor the outcomes of the interaction of the electron with an adsorbate.

Keywords:

Mass spectrometric imaging; Plasmonic hot electron transfer; Plasmon-induced interfacial charge-transfer transition; Redox activity; Protonation and deprotonation

INTRODUCTION

View Article Online
DOI: 10.1039/D5SC02632F

The bright-field imaging of a regular optical microscope with a field view of a few millimeters is a morphology-based technique that has been widely used in histopathological assessment and clinical diagnosis.[1-3] In this technique, nucleic acids or cytoplasm and extracellular matrix are stained with haematoxylin and eosin (H&E) respectively, to unravel different types of cells and their morphological changes.[4-6] The high morphological similarities of different cells are challenging for the identification of abnormal cells and may lead to discordant conclusions among different pathologists.[7-9] These difficulties have driven the development of alternative staining-free techniques in histopathology, including photoacoustic microscopy (PAM),[10-12] phase detection microscopy (PDM)[13-15] and stimulated Raman scattering microscopy (SRSM)[16-18] as the results of the advancement of modern laser technologies. PAM and PDM are ensemble-averaged techniques that represent the overall optical, thermal, elastic, morphological and mechanical properties of objects.[19-21] In contrast, SRSM has molecular specificities dependent on vibrational motions of chemical bonds of molecules.[22-24] However, the small field view makes it still difficult to localize the boundary between normal and diseased regions by using these microscopic techniques.

Mass spectrometric (MS) imaging has emerged as a new approach that can provide not only molecular identities (including accurate molecular weights, element compositions and isotopic features) but also spatial distributions of various molecules, which can clearly classify precancerous, cancerous and normal regions in tissue slices.[25-27] It generates a color-contrast image with a wide field view up to several centimeters in which different colors and intensities represent different species and quantities, to aid digitalized histopathological analysis.[28-30] DESI (desorptive electrospray ionization)[31-33] and MALDI (matrix-assisted laser desorption ionization)[34-36] are two representative mass spectrometric techniques that utilize either a liquid solvent beam or a laser beam to scan across tissue slices. In nature, both DESI and MALDI are based on the non-specific protonation/deprotonation mechanism by which neutral molecules are converted into positive or negative ions. Non-protonated and non-deprotonated

View Article Online
DOI: 10.1039/D5SC02632F

organic molecules and inorganic metal ions with various redox activities that are crucial for spatiotemporal regulation of oxidization-reduction homeostasis cannot be identified. The broad diversities of the composition of biological systems require a different technique.

We are describing a photoelectron-driven ionization paradigm for reactive mass spectrometric imaging of organic and metallic metabolites. Images are acquired from Au nano-structural ultrathin films that are prepared by atomic sputtering deposition on simple ITO glass slides. It takes the advantages of plasmonic hot electron transfer for specific ionization and localization with high spatial resolution. Nanocrystalline Au thin films have presented enormous scientific interest because of the attractive novel surface features and quantum size properties.[37, 38] By blotting tissue slices on Au sputtered ITO glass slides, we are aimed to achieve enhanced hot electron transfer by plasmon-induce interfacial charge-transfer transition (PICTT) that directly excites electrons from Au atoms to strongly coupled electron receptors. Transfer of photoelectrons to those molecules with specific reduction potential is independently on the heating of the laser beam. Then heating-induced co-evaporation and co-ionization of nearby co-existing molecules in regular MALDI MS are eliminated, which enables high spatial resolution. The highly reactive plasmonic electrons not only facilitate the mass spectrometric imaging of organic metabolites but also metal ions through *in situ* surface chemical reactions that can generate coordinative species for the evaporation of metal ions. The PICTT MS technique has been applied to the imaging of brain slices of a 4T1 breast tumor-bearing mouse.

It should be noted that the charge and energy flow at the plasmonic metal–molecule interface is central to the energy conversion from light illumination to chemical reactions. Understanding the plasmonic excitations of adsorbed molecules has been challenging. Although numerous electronic and surface effects occurring at the plasmonic metal–molecule interface have been observed, including chemical interface damping (CID), Landau damping, or plasmonic vibrational pumping, as well as

View Article Online
DOI: 10.1039/D5SC02632F

adsorbate-induced surface resistivity and desorption induced by electronic transitions (DIET)[39], direct experimental evidences are needed to delineate the roles of all these effects in charge and energy flow at the plasmonic metal-molecule interface. Mass spectrometry is a mass and charge (*m/z*)-dependent technique in which positive or negative ions can be detected. With the set-in equipped Nd^{3+}:YAG pulsed laser (355 nm, 3 ns pulse width), it is convenient to detect the products of charge transfer and plasmon-driven chemical reactions upon laser illumination. It is a robust tool to monitor various outcomes that stem from interactions of electrons and adsorbates, such as plasmonic chemical reactions, electronic and vibrational excitation of adsorbed molecules or desorption from the plasmonic metal surfaces.

EXPERIMENTAL

Sample preparation for mass spectrometric imaging. Reagents and apparatus were described in Notes S1. All animal procedures were performed in accordance with the Guidelines for Care and Use of Laboratory Animals of Guangxi University and approved by the Animal Ethics Committee of Guangxi University prior the research. The code of the related animal experimental ethical inspection form of Guangxi University is GXU-2022-303. Preparation of mouse brain was described in Notes S2. ITO glass slides were sputtered with Au nanoparticles. Briefly, ITO glass slide was put in the Cressington Sputter Coater 108 auto (Watford, UK), in which a cool, fine-grain auto-sputtering is achieved with a very efficient DC magnetron head. The sputtering current, time, pressure of Ar gas and distance between the sample plate and the Au target were set as 10 mA, 40 s, 0.08 mbar and 4 cm, respectively. According to the operation manual provided by the manufacturer, the deposition rate is 1.2 $nm \cdot s^{-1}$ under these conditions. When the current, distance and gas pressure are maintained, the sputtering time directly changes the thickness of the Au film. Considering the size distribution, plasmonic efficiency of resultant nanoparticles and the consumption of Au, the deposition time was eventually decided as 40 s that offers a uniform coating with a thickness around 50 nm. The sputtering is a physical vapor

View Article Online
DOI: 10.1039/D5SC02632F

deposition process at the atomic level, in which collisions cause atoms near the surface being expelled. The expelled atoms are then deposited on the ITO glass slides. Electron microscopic images were acquired on a Hitachi SU8200（Tokyo, Japan）scanning electron microscopy (SEM). It shows the gold layer growth to be running over the ITO glass slides uniformly.

Mass spectrometric imaging. Mass spectrometric analysis and bio-imaging were performed on a Bruker Daltonics timsTOF Flex MALDI 2 (Billerica, USA) mass spectrometer. It was calibrated with ESI-L low concentration tuning mix in negative ion mode ranging from *m/z* 50 to 1300 (Notes S3). Fig. S1 shows a representative calibration result. The mass error is usually less than 0.3 ppm. The mass spectrometer is equipped with two Nd^{3+}: YAG high repetition laser heads (355 nm, 266 nm) and the laser beam size was set at ~5 μm. When only laser at 355 nm was turned on, the laser influx, pulse width and fire rate were set as 70%, 3 ns and 10000 Hz, respectively. When the second ultraviolet laser at 266 nm was also turned on along with the first laser at 355 nm, the fire rate was switched from 10000 Hz to 1000 Hz. For simple mass spectrometric analysis of standard free fatty acids, lipids or homogenized brain tissues (Notes S4), the samples were mixed with equal volume of 9-AA solution before spotting on the Au sputtered ITO glass slide. For bio-imaging of tissue slices, tissue slices were blotted on the thin film of Au nanoparticles that were sputtered on the ITO glass slides. Then tissue slices were sprayed with the solution of 9-AA. All mass spectrometric imaging was acquired from brain tissue slices of a 4T1 tumor-bearing BALB/c adult female nude mice weighting 15~17 g. The spraying of auxiliary matrix materials was described in Notes S5. The pixel size was set as 20 μm x 20 μm and laser shots for each pixel were set as 200. Mass spectrometric data sets were processed with SCiLS Lab software (Bruker Daltonics, USA) for the reconstruction of images. Different colors represent different intensities of ions in which the highest and the lowest intensities are shown as white and black colors, respectively.

View Article Online
DOI: 10.1039/D5SC02632F

A computational tool for the comparison of organic metabolites and metal ions in cancerous and normal tissue regions. Mass spectrometric data was uploaded to search against human metabolite database (HMDB). All *m/z* values were either directly subjected to searching databases or processed for the losses of H^+/H atoms (1.0078) before database searching. A computer program called Comparedoxome v1.0 was developed to analyze the output results of HMDB searching. Comparedoxome is aimed to compare the normal and cancerous redoxomic metabolites. It can list the species that only exist in normal or cancerous samples. Comparedoxome is written with python 3.11. It can be freely run or downloaded from Supporting Information Notes S6.

RESULTS AND DISCUSSION

Hot electron transfer-directed ionization and the decay of gold plasmon. Mass spectrometry is based on the detection of gaseous ions with either positive or negative charges. The surface plasmon resonance (SPR) of metallic nanostructures has been applied to photocatalysis,[40] photovoltaics,[41] and photodetectors[42] by increasing light absorption[43] or plasmon induced charge transfer from the excited metal to adsorbed molecules.[44, 45] It suggests the possible utilization of plasmonic metal nanostructures as light absorbers that can generate hot electrons for *in situ* soft ionization of redox active species in mass spectrometry. By using 9-AA as an example, Figure 1 illustrates the three ways for photoelectron transfer and computational method is described in Notes S7. Figure 1 (A) represents the conventional plasmon induced hot-electron transfer (PHET) mechanism, by which plasmons decay into hot electron–hole pairs with a broad distribution of initial electron and hole energies within the metal via Landau damping in a time scale of a few to tens of femtoseconds.[46] Rapid electron-electron scattering in a time scale of hundreds of femtoseconds is the major problem that limit the efficiency of PHET.[47] Alternative approach is the direct metal-to-molecule interfacial charge transfer transition (DICTT) shown in Figure 1 (B) in which the light illumination directly excites an electron from the metal into the lowest unoccupied molecular orbital (LUMO) of adsorbate molecules.[48] Such interfacial transitions are usually very weak

View Article Online
DOI: 10.1039/D5SC02632F

due to inefficient light-harvest. Enhanced hot electron transfer is expected to achieve by the combination of strong light absorbing power of plasmonic transitions with the superior charge-separation properties of the DICTT mechanism.[49] It has been reported that decreasing plasmonic particle size can increase the rate of hot electron transfer and reduces the barrier of hot electron transfer.[50] In this work, Au nano-structural ultrathin films are developed by atomic sputtering deposition on ITO glass slides. Figure 1 (C) illustrates the **plasmon**-induced metal-to-molecule **interfacial charge transfer transition** (PICTT) pathway on such ultrathin Au sputtered film for mass spectrometric imaging. PICTT enables the decay of plasmons by direct excitation of electrons from metal atoms to the lowest unoccupied molecular orbital (LUMO) of strongly coupled electron receptors in tissue sections that are blotted on the Au sputtered ITO thin film. Fig. S2 (A) and (B) represents the images of scanning electron microscope (SEM) of Au sputtered ITO glass slides. It is shown Au nanoparticles deposited within 40 s have been uniformly distributed on the ITO glass slide and the coefficient of variation is about 8% in Fig. S2 (C). Sizes of nanoparticles are mainly between 10 nm and 100 nm and 5% nanoparticles are more than 100 nm as shown in Fig. S2 (D). Plasmonic chemistry is closely related with sizes of nanoparticles. It has been reported that metal nanoparticles with diameters between 5 nm and 100 nm are most favored for plasmon-driven chemistry, to which the sputtered Au nanoparticles are in accordance.[39] Au sputtered ITO slides with about 50 nm sizes that are deposited within 40 s generate strong signal intensities with the lowest signal-to-noise (S/N) ratio compared with that deposited with 20 s and 60 s in Fig. S2 (E). Eventually, the deposition time of 40 s was chosen for the downstream experiments. Fig. S3 illustrates the element composition of ITO glass slides by energy dispersive X-ray spectroscopy (EDS).

Notably, the electron configuration of Au is [Xe] $4f^{14}$ $5d^{10}$ $6s^{1}$. It is implicated that the adding or removing of a single electron to or from the Au adatoms should lead to the generation of stable Au^{-} or Au^{+} ions with fully occupied or empty 6s-derived states. This unique character makes the Au atom a robust internal reference that points to the direction of electron flow. On surfaces, electron transfer and the charge state of

View Article Online
DOI: 10.1039/D5SC02632F

adatoms are determined by substrates and co-adsorbates.[51] Upon the irradiation of a pulsed ultraviolet laser on sputtered Au nanoparticles, plasmonic hot electrons can either transfer to Au atoms and switch neutral Au adatoms to negatively charged Au^- ion at *m/z* 196.9645 (expected at *m/z* 196.9665, error 0.0020) in Figure 2 (A) and (B), or transfer to adsorbed organic molecules, dependently on reduction potential differences and bias voltages between sample plate and the aperture. Figure 2 shows the first mass spectrometric evidence for the transfer of plasmonic hot electrons generated by plasmon decay to gold (Au) atoms themselves. When samples are directly spotted on surfaces of Au sputtered ITO thin film, neutral molecules are ionized through a PICTT route and converted into radical anions that undergo subsequent electron-driven bond cleavages. In such case, excited hot electrons transfer to charge deficient atoms of adsorbed molecules with specific reduction potentials. Figure 2 (A) shows the mass spectrum of the negative ion of a standard compound free fatty acid C20:1 resulting from the capture of a hot electron at the C atom of the carboxyl group. Resultant radical anions are highly reactive and the radical center can initiate the homolytic cleavage of α-positioned O-H bond, which generates the ion at *m/z* 309.2784 (error: 0.0002). As for the standard compound phosphatidylglycerol, ions at *m/z* 773.5339 (error: 0.0006) and *m/z* 281.2484 (error: 0.0012) are produced from two pathways respectively, in which hot electrons are captured by either P atom of the phosphate group or C atom of the carboxyl group followed with a homolytic cleavage of C-O bond as shown in Figure 2 (B). MS spectra of other compounds are listed in Fig. S4. Clearly, detected acidic metabolites are produced through the electron transfer ionization that causes the loss of a H atom instead of a proton. In this case, both the products of electron transfer to plasmonic Au nanoparticles themselves and adsorbed lipids are observed in Figure 2. The efficiency of hot electron transfer ascribes to sputtered plasmonic Au nanoparticles. In comparison with general MALDI, C20:1 was used as an example to demonstrate the enhanced ionization via plasmonic hot electron transfer in Fig. S5. The absolute intensity of C20:1 generated with PICTT MS is about 8 times more than that of general MALDI MS. It is shown the detection limit of PICTT MS can be down to 10 fmol and signal-to-noise ratio (S/N)

View Article Online
DOI: 10.1039/D5SC02632F

is about 56.

PICTT MS imaging and proton coupled electron transfer. In order to avoid direct laser ablation, an auxiliary material is uniformly sprayed on the tissue slices and co-crystalized with endogenous metabolites for downstream mass spectrometric analysis. When a brain tissue slice is blotted on the Au sputtered ITO glass slides and coated with the auxiliary matrix material, the detection of Au^- is determined by differences in reduction potentials and abundances between plasmonic Au nanoparticles and compounds present in local tissue regions. Figure 3 (A) shows the mass spectrometric image of a non-auxiliary matrix coated brain slice "O" of the 4T1 breast tumor-bearing BALB/c adult female nude mouse on Au sputtered ITO glass slide, which is usually used as a model of brain metastasis of breast cancer. It is noted that Au^- ions were detected in the region of cortex and corpus callosum, meaning electrons can transfer to Au nanoparticles in the local regions of this brain tissue slice, or the concentration of redox active endogenous metabolites is low in this region. The non-continuous intensities of Au^- ions implicates heterogenous composition that can compete with Au^- nanoparticles for electron capture. In contrast, the absence of Au^- ions in other regions indicates highly redox active regions that can easily capture hot electrons. The redox signaling regulates various neurological processes such as neurotransmission and homeostasis through specific oxidation/reduction reactions.[52] These dissected redox active and inactive regions provide new experimental evidences for the elucidation of the redox balance in brain.

Figure 3 (B) shows the mass spectrometric image of an auxiliary matrix coated brain slice "X" of the 4T1 breast tumor-bearing BALB/c adult female nude mouse on Au sputtered ITO glass slide. Au^- ions were not detected because of the redox activity of abundant 9AA. As shown in Figure 3 (C), the electron acquired by 9-AA is delocalized, which stabilizes resultant 9-AA radical anions. In the presence of such auxiliary matrix material, there is a proton coupled electron transfer (PCET) that facilitates the deprotonation and detection of organic acids in negative ion mode in

View Article Online
DOI: 10.1039/D5SC02632F

addition to hot electron transfer ionization depicted in Figure 2. The ionization efficiency of acidic metabolites is increased in PICTT route, which provides stronger signals than regular MALDI MS imaging. Additionally, compared with non-specific regular protonation/deprotonation-based ionization approach, electron transfer ionization is specific. Chemical and environmental properties of redox active metabolites present in tissue sections may cause differential hot electron transfer, which is associated with redox activities. The PICTT MS generates different images than regular MALDI MS because only those metabolites with specific reduction potential can be ionized and detected. This maybe the reason why PICTT MS provides higher spatial resolution than that of regular MALDI, which uses non-specific protonation/deprotonation ionization. Without selectivity, all compounds maybe overlapped and the spatial resolution maybe destroyed. Notably, in PICTT MS, the reduction of compounds can be affected when the bias voltage between the sample plate and the aperture located in the ion source chamber of the mass spectrometer is adjusted. Electron transfer is also determined by differences in reduction potentials of co-existing compounds. Although redox inactive compounds cannot be ionized through electron transfer pathway, those compounds can still be detected through the deprotonation pathway if basic auxiliary matrix materials are used. Figure 3 (D) shows the comparison of PICTT MS and MALDI MS imaging of two adjacent slices of a 4T1 mouse brain. Long chain fatty acids C20:1, C16:0, phospholipids PG (C36:2) and citrate were used as examples. Because of the dissociation equilibrium, both deprotonated and non-deprotonated species of these acidic metabolites are present. MALDI MS can only detect deprotonated species but PICTT MS can provide additional electron transfer ionization route to those non-deprotonated species. PICTT MS enhances the detection of those acidic metabolites, in particular for those weak acids such as citric acid. The PICTT MS imaging of other metabolites was shown in Fig. S6. It should be noted the coordination of functional groups of metabolites with nanoparticle surfaces may change plasmonic properties and quench plasmonic electrons. Such features provide a way to sense the presence of such compounds in specific pixels.

View Article Online
DOI: 10.1039/D5SC02632F

PICTT MS imaging of zwitterions. As we know, it is impossible for MALDI MS to detect zwitterions because those species do not have net charges. In contrast, PICTT MS can ionize those species by plasmonic hot electron transfer. Figure 4 (A) illustrates the ionization mechanisms of ions at *m/z* 300.0386, 213.0062, 225.0064 and 256.9968, which were identified as cinnabarinic acid (expected 300.0382, error: 0.0004 Da), indoxyl sulfate (expected 213.0096, error: 0.0034), quinolin-2-yl hydrogen sulfate (expected 225.0096, error: 0.0034 Da) and hydroxylated quinolin-2-yl hydrogen sulfate (expected 256.9994, error: 0.0026 Da), respectively. As shown in Figure 4 (B), the excitation of electrons from plasmonic Au atoms to the LUMO of adsorbed molecules leads to the generation of negative ions that can be detected with mass spectrometry in negative ion mode. Instead, deprotonated species of those zwitterions were not detected or the detected signals were very low (data not shown). Although electron transfer (ET) can also occur on ITO without sputtered Au atoms upon laser irradiation, the low ionization efficiency causes weaker signals than that of Au sputtered ITO. Overall, detected ions (n=806) with intensity counts more than 30000 have been subjected to statistic analysis. Significant higher intensity ratios of ions detected on Au-sputtered ITO than that of non-sputtered ITO slides have been found at a 95% confidence level (P-value: $6x10^{-24} < 0.05$). Intensity ratios of these ions at *m/z* 300.0382, 213.0096, 225.0096 and 256.9994 acquired with PICTT on plasmonic Au nanoparticles over that of ET on ITO are 1.2, 1.3, 1.3 and 1.2, respectively. Notably, in current MALDI MS, even if those ions resulting from electron transfer are detected, those ions cannot be identified due to the lack of the recognition of such electron transfer ionization mechanism. Cinnabarinic acid is the endogenous metabolite of tryptophan-kynurenine pathway associated with brain function and neurotransmission. It activates metabotropic glutamate (mGlu) receptors[53] as well as NF-kappaB pathway by binding with aryl hydrocarbon receptor (AhR).[54] Reduced cinnabarinic acid levels in prefrontal cortex (PFC) was reported in pathophysiology of schizophrenia.[55] Figure 4 (B) reveals the spatial distribution of indoxyl sulfate that was also reported as the agonist of aryl hydrocarbon receptor (AhR) by using PICTT MS imaging. It has been

View Article Online
DOI: 10.1039/D5SC02632F

found that PICTT MS imaging has the resolution that can clearly distinguish the spatial distribution of cinnabarinic acid and indoxyl sulfate as well as the slight locational changes of quinolin-2-yl hydrogen sulfate caused by hydroxylation. Although the function of quinolin-2-yl hydrogen sulfate and its hydroxylation remains unknown, their co-localization facilitates the understanding of a concerted redoxome. On the contrary, regular MALDI MS is not able to identify zwitter ions with no net charges and images acquired with ET on ITO without plasmonic Au nanoparticles generates lower signals.

Two-electron transfer ionization of positive ions in PICTT MS imaging. In regular MALDI MS, positive ions can only be detected in positive ion mode. PICTT MS can detect both negative and positive ions in the negative ion mode through multiple electron transfer. There are some positive ions such as phosphatidylcholine (PC or GPCho) shown in Figure 5 (A) that cannot be detected by protonation/deprotonation-based MALDI MS in negative ion mode. We are demonstrating that this proposed technique provides a way to transform those compounds through two-electron transfer. The capture of one hot electron neutralizes positively charged PC and the second hot electron converts resultant zwitterion into a negative ion at *m/z* 908.6386 (expected 908.6381, error: 0.0005) that can be detected in the negative ion mode of mass spectrometry. It has been noted those glycerophosphocholines have various isomers with different combinations of fatty acids with varying lengths and saturation at C1/C2 positions of the glycerol backbone or α-positions of the two furan rings.

The fragment ion at *m/z* 907.6351 (expected 907.6308, error: 0.0043) resulting from electron-driven homolytic cleavage of O-H bond verifies the presence of O-H bond. PICTT MS imaging shows that both parent ion at *m/z* 908.6386 and fragment ion at *m/z* 907.6351 has exactly the same spatial distribution as shown in Figure 5 (B). Desaturation causes changes in the locations of ions at *m/z* 905.6152 and 903.5996. It is shown that PICTT MS imaging can clearly locate the spatial changes caused by

sequential desaturations in Figure 5 (B). PICTT MS imaging of other PCs are shown in Fig. S7. Without plasmonic Au nanoparticles, ET on ITO generates images that are not only weaker but also overlapped. Through simple ET on ITO, images of the ion at *m/z* 907.6308 and the ion at *m/z* 905.6152 are almost the same. It can only detect locational changes of the ion at *m/z* 903.5996 generated by two desaturations.

PICCT MS imaging of negative ions. As for acidic metabolites, there are dissociation equilibrium in which both neutral, dissociated negative species and positive protons are co-existed. In regular MALDI MS, negative ions can be directly detected in the negative ion mode. But in PICTT MS, neutral species can be detected through electron transfer ionization in addition to negative species. Then PICTT MS provides stronger signals than regular MALDI MS. Glycosphingolipids (GSLs) are ubiquitously expressed carbohydrate derivatives abundant in the nervous system, which contain a ceramide backbone with varying acyl chain and a glycan moiety.[56] Various sulfatide are used as examples to demonstrate the capability of PICTT MS for the detection of negative ions. Sulfatides are representative members of the GSLs family that account for almost one third of myelin lipids. They have cell type-specific structural variations with different acyl chain lengths and hydroxylation. In physiological condition, sulfatides are negatively charged because of the dissociation equilibrium. Mass spectrometric analysis of carbohydrate derivatives is challenging because these species are polar, hydrophilic and poorly retained on reversed-phase high-performance liquid chromatography (RP-HPLC) columns coupled with mass spectrometers. PICTT MS provides a way to detect those species without RP-HPLC. Figure 6 clearly shows the regional specific distributions of a non-hydroxylated and hydroxylated sulfatide (C38:1) with PICTT MS imaging that are at *m/z* 834.5765 and 850.5714, respectively. It is shown PICTT MS provides stronger signals and better spatial resolution for the detection of locational changes caused by the hydroxylation than that of regular MALDI MS. Activation of peroxisome proliferator-activated receptor α (PPARα) may increase the expression of sulfatides and promote the migration and invasion of tumors in breast cancer.[57] But the function of the

View Article Online
DOI: 10.1039/D5SC02632F

hydroxylation of sulfatide remains unknown. PICTT MS also shows the locational changes caused by chain lengths and desaturations such as ions at *m/z* 890.6391, 888.6235 and 778.5139 while regular MALDI MS provides images with lower signals and resolution. In particular, accumulated psychosine sulfate at *m/z* 540.2843, a minor compound in normal brain, was found in the brain of 4T1 breast tumor-bearing BALB/c adult female nude mouse. The accumulation of psychosine sulfatide indicates the insufficient activity of lysosomal galactosyl-ceramidase (GALC) in breast tumor-bearing mouse that is the only enzyme capable of hydrolyzing psychosine. Uridine diphosphate galactose/glucose was detected at *m/z* 565.0472, from which galactose is transferred to ceramides by ceramide galactosyltransferase (UGT8) so as to form galactosyl ceramides (GalCer) and then to sulfate by GalCer sulfotransferase (GST). High UGT8 expression has been thought to be closely related to the tumor grade and size in patients with basal breast cancer.[58] Uridine diphosphate-N-acetylgalact/glucosamine was detected at *m/z* 606.0738 with different regional distribution. It is a nucleotide sugar used by glycosyltransferases for the biosynthesis of glycoproteins, sulfatides, cerebrosides and glycoRNA.[59-61]

Application of PICTT MS to profile metabolic redoxome. The brain of a 4T1 breast tumor-bearing mouse and a control normal mouse were homogenized and mixed with 9-AA. The mixtures were spotted on the Au sputtered ITO slide or non-Au sputtered ITO slide, respectively. Detected ions in cancerous or normal mouse brain homogenates were listed in Table S1 and Table S2, respectively. There are 66 metabolites indicated with red color in Table S1 were only detected in the brain of a 4T1 breast tumor-bearing mouse. Figure 7 (A) shows the spatial distribution of these 66 metabolites in the brain slices. It was found that these metabolites are mostly enriched in spinal cord, medulla oblongata, cerebral cortex, leptomengines, frontal lobe, parietal lobe and hippocampus regions of functional importance. Leptomeningeal metastasis has been diagnosed in breast cancer patients.[62] The leptomeninges (LM) are cerebrospinal-fluid-filled tissues surrounding the brain and spinal cord that are involved in various pathologies. It has not been understood how the metastatic invasion occurs

in the LM microenvironment that is anatomically and immunologically sequestered with poor nutrients. Recently, Sipkins research group has exploited neural signaling pathways for bone-to-meninges metastasis that bypasses the blood brain barrier.[63] They found breast cancer cells can overexpress cell surface receptor integrin α 6 and invade the LM by traversing the outer surface of blood vessels that connect the adjacent vertebral and skull bone marrow with the central nervous system meninges. And then resident meningeal macrophages are stimulated to secrete glial-derived neurotrophic factor (GDNF) for the supporting of tumor growth. Our experimental results provide the molecular anatomic support for such metastasis from vertebral bone marrow (BM)-to-leptomeninges (LM). In particular, Figure 7 (B) clearly shows the invasion course started from the over-production of phospholipids at *m/z* 716.5211, 727.5263, 742.5370, 749.4991, 762.5058, 766.7367, 772.5835, 851.5792 and 864.5702. This is in accordance with the report that GDNF regulates lipid metabolism and glioma growth.[64]

Over-produced inositol trisphosphate (IP3) was observed in the brain of 4T1-tumor-bearing mouse as shown in Figure 7 (C), which is a second messenger controlling many cellular processes through the generation of internal calcium signals. It has been reported IP3-dependent nuclear calcium signals regulate angiogenesis and cell motility in triple negative breast cancer.[65] And the down-regulation of IP3 receptor decreases breast cancer cell migration through an oscillatory Ca^{2+} signal.[66] The appearance of IP3 in the brain of 4T1-tumor-bearing mouse implicates the invasion of the breast tumor to the brain.[67]

***In situ* plasmonic chemical reactions and PICTT MS imaging of metal ions.** In addition to organic molecules, inorganic metal ions are always present in cells in forms of various metal-binding enzymes or metalloproteins to mediate electron transportation.[68, 69] Currently, mass spectrometric imaging has been developed mainly for organic molecules. It is still technically challenging for *in situ* bio-imaging of metal ions. Secondary ion mass spectrometry (SIMS) is a choice.[70] But it generates extensive background interferences because it applies energetic primary particles

View Article Online
DOI: 10.1039/D5SC02632F

(electrons, ions or photons) to bombard with solid surfaces of samples for ionization and dissociation.[71] We take the advantage of PICTT MS and develop a plasmonic electron-based soft ionization technique for bio-imaging of metal ions in tissues. By using iohexol as an auxiliary matrix, the illumination of laser pulse (3 ns pulse width, 355 nm) generates iodide ions (Fig. S8) on Au sputtered ITO slides that can form clusters with various metal ions for mass spectrometric detection. Figure 8 shows the mass spectrometric imaging of Na^+, K^+, Ca^{2+}, Cu^{2+}, Fe^{2+} and Zn^{2+} ions as well as their isotopes in a brain section of a 4T1 tumor-bearing mouse. There is aberrantly high abundance of these metal ions than that in normal mouse brain (Fig. S9), in particular for Na^+ and K^+ ions. It has been found that voltage-activated sodium channels (VGSCs) does be selectively upregulated in metastatic breast cancer to drive Na^+ influx, generate action potentials and proceed propagation.[72] Similarly, the expression of voltage-gated potassium channel is also significantly increased in late stage breast cancer.[73] In addition to Na^+ and K^+, intracellular Ca^{2+} signaling is a critical factor in breast cancer metastasis. It has been considered as oncogenic markers of breast cancer.[74] Although Zinc is vital in functions of many proteins for the recognition of specific DNA sequences and regulation of gene transcription, it can be involved in invasive behavior of breast cancer cells. Lots of reports have shown that zinc levels are higher in breast tumors than in normal breast tissues.[75] Accordingly, Figure 8 shows increased levels of Na^+, K^+, Ca^{2+}, Mg^{2+} and Zn^{2+} in 4T1tumor-bearing mouse brain. Compared with normal mouse brain (Fig. S10), increased transition metal ions such as Fe ions have been observed. But there is no obvious changes in copper ions. By non-covalent coordination with proteins, these transition metals are involved in electron transfer or molecular reduction reactions such as the deactivation of reactive oxygen species (ROS) and mitochondrial energy production.

CONCLUSIONS

PICTT MS provides an electron-driven ionization paradigm for mass spectrometric imaging of organic and metallic metabolites. It is based on the plasmon-induced interfacial charge-transfer transition that enables the transfer of plasmonic electrons to

strongly coupled redox active species in tissue sections blotted on Au sputtered ITO slides. In combination with auxiliary matrix material, PICTT MS provides a unique way for simultaneous localization of organic and inorganic metal ions that cannot be protonated or deprotonated in the negative ion mode in current MALDI MS. Highly reactive plasmonic hot electrons are efficient for rapid *in situ* chemical reactions that can generate coordinative species for mass spectrometric analysis of metal ions. Although photo-induced electron transfer (ET) can also occur on simple ITO slides upon laser irradiation, the ionization efficiency is low without plasmonic Au nanoparticles. PICTT MS paves a new way to tackle with the nature of the electronic excitations at the plasmon–molecule interface because it can directly monitor the outcomes of the interaction of the electron with an adsorbate.

Associated Content

Supporting Information

This material is available free of charge via the internet.

Author Information

Corresponding Author

Email: hyzhong@gxu.edu.cn

Author Contributions

Hongying Zhong developed the original concept, designed the experiments, analyzed the data and wrote the manuscript. Shao Chang and Xin Zhou performed all experiments. Xin Zhou developed the computational program RedoxomeMap v 1.0. Anji Gao analyzed data, elucidated and drew mechanisms. Shao Chang, Xin Zhou and Anji Gao contribute equally to this work. Yixiang Luo analyzed part of the mass spectrometric data. Yujia Shan developed the computational program Comparedoxome v 1.0. Lin Zhang and Zhengwei Gui were involved in breast tissue analysis. Xincheng Huang, Xiaoyuan Hu and Tianci Huo were involved in mass spectrometric analysis and imaging. Linhui Liu was involved in sample preparation

View Article Online
DOI: 10.1039/D5SC02632F

and instrument operation.

Acknowledgements

Authors thank the final support from Guangxi Science and Technology Major Program （AA23073019, AB25069175）, National Natural Science Foundation of China (NSFC22474028), Guangxi Natural Science Foundation (2025GXNSFDA069026), as well as research Funds of Guangxi University and Central China Normal University.

REFERENCES

1. N. Naik, A. Madani, A. Esteva, N. S. Keskar, M. F. Press, D. Ruderman, D. B. Agus and R. Socher, *Nat. Commun.,* 2020, **11**, 5727.
2. X. Pan, Y. Lu, R. Lan, Z. Liu, Z. Qin, H. Wang and Z. Liu, *Comput. Electr. Eng.,* 2021, **91**, 107038.
3. G. Shamai, A. Livne, A. Polónia, E. Sabo, A. Cretu, G. Bar-Sela and R. Kimmel, *Nat. Commun.,* 2022, **13**, 6753.
4. A. H. Fischer, K. A. Jacobson, J. Rose and R. Zeller, *Cold Spring Harb. Protoc.,* 2008, **5**, pdb-prot4986.
5. M. J. Pilling, A. Henderson, J. H. Shanks, M. D. Brown, N. W. Clarke and P. Gardner, *Analyst*, 2017, **142**, 1258-1268.
6. G. Musumeci, *J. Histol. Histopathol.*, 2014, **1**, 1-3.
7. T. A. A. Tosta, P. R. de Faria, L. A. Neves and M. Z. do Nascimento, *Artif. Intell. Med.*, 2019, **95**, 118-132.
8. C. Munien and S. Viriri, *Comput. Intell. Neurosci.*, 2021, **2021,** 5580914.
9. J. Zheng, H. Zhang, S. Li, Z. Kang, F. Zheng, Q. Yao and M. Chen, *BMC Cancer*, 2023, **23**, 1193.
10. T. T. Wong, R. Zhang, P. Hai, C. Zhang, M. A. Pleitez, R. L. Aft, D. V. Novack and L. V. Wang, *Sci. Adv.*, 2017, **3**, e1602168.
11. L. Kang, X. Li, Y. Zhang and T. T. Wong, *Photoacoust.*, 2022, **25**, 100308.
12. R. Cao, S. D. Nelson, S. Davis, Y. Liang, Y. Luo, Y. Zhang, B. Crawford and L. V. Wang, *Nat. Biomed. Eng.*, 2023, **7**, 124-134.

13. M. Töpperwien, F. van der Meer, C. Stadelmann and T. Salditt, *Proc. Natl. Acad. Sci.*, 2018, **115**, 6940-6945.
14. Y. Rivenson, T. Liu, Z. Wei, Y. Zhang, K. de Haan and A. Ozcan, *Light Sci.Appl.*, 2019, **8**, 23.
15. M. Eckermann, B. Schmitzer, F. van der Meer, J. Franz, O. Hansen, C. Stadelmann, and T. Salditt, *Proc. Natl. Acad. Sci.*, 2021, **118**, e2113835118.
16. C. W. Freudiger, W. Min, B. G. Saar, S. Lu, G. R. Holtom, C. He, J. C. Tsai and J. X. X. S. Kang, *Science*, 2008, **322**, 1857-1861.
17. D. A. Orringer, B. Pandian, Y. S. Niknafs, T. C. Hollon, J. Boyle, S. Lewis, M. Garrard, S. L. Hervey-Jumper, H. J. L. Garton, C. O. Maher, J. A. Heth, O. Sagher, D. A. Wilkinson, M. Snuderl, S. Venneti, S. H. Ramkissoon, K. A. McFadden, A. Fisher-Hubbard, A. P. Lieberman, T. D. Johnson, X. S. Xie, J. K. Trautman, C. W. Freudiger and S. Camelo-Piragua, *Nat. Biomed. Eng.*, 2017, **1**, 0027.
18. Y. S. Zhang, J. Yao, C. Zhang, L. Li, L. V. Wang and Y. Xia, *Angew. Chem. Int. Ed.,* 2014, **126**, 8237-8241.
19. L. V. Wang and L. Gao, *Ann. Rev. Biomed. Eng.*, 2014, **16**, 155-185.
20. Y. Yang, Z. Liu, J. Huang, X. Sun, J. Ao, B. Zheng, W. Chen, Z. Shao, H. Hu, Y. Yang and M. Ji, *Theranostics*, 2023, **13**, 1342.
21. J. L. Ganoza-Quintana, F. Fanjul-Vélez and J. L. Arce-Diego, *Appl. Sci.*, 2021, **11**, 6142.
22. R. He, Y. Xu, L. Zhang, S. Ma, X. Wang, D. Ye and M. Ji, *Optica*, 2017, **4**, 44-47.
23. M. Ji, D. A. Orringer, C. W. Freudiger, S. Ramkissoon, X. Liu, D. Lau, A. J. Golby, I. Norton, M. Hayashi and N. Y. R. Agar, G. S. Young, C. Spino, S. Santagata, S. Camelo-Piragua, K. L. Ligon, O. Sagher and X. S. Xie, *Sci. Transl. Med.*, 2013, **5**, 201ra119-201ra119.
24. Z. Liu, W. Su, J. Ao, M. Wang, Q. Jiang, J. He, H. Gao, S. Lei, J. Nie, X. Yan, X. Guo, P. Zhou, H. Hu and M. Ji, *Nat. Commun.*, 2022, **13**, 4050.
25. Z. Takats, J. M. Wiseman, B. Gologan and R. G. Cooks, *Science*, 2024, **306**, 471-473.
26. D. S. Cornett, M. L. Reyzer, P. Chaurand and R. M. Caprioli, *Nat. Methods*, 2007,

View Article Online
DOI: 10.1039/D5SC02632F

4, 828-833.

27. M. Aichler and A. Walch, *Lab. Invest.*, 2015, **95**, 422-431.
28. K. Chughtai and R. M. Heeren, *Chem. Rev.*, 2010, **110**, 3237-3277.
29. C. Bamberger, U. Renz and A. Bamberger, *J. Am. Soc. Mass Spectrom.*, 2011, **22**, 1079-1087.
30. K. Chughtai and R. M. Heeren, *Chem. Rev.*, 2010, **110**, 3237-3277.
31. D. Calligaris,D. Caragacianu, X. Liu, I. Norton, C. J. Thompson, A. L. Richardson, M. Golshan, M. L. Easterling, S. Santagata, D. A. Dillon, F. A. Jolesz and N. Y. Agar, *Proc. Natl. Acad. Sci.*, 2014, **111**, 15184-15189.
32. N.M. Morato and R. G. Cooks, *Acc. Chem. Res.* 2023, **56**, 2526-2536.
33. T. Soudah, A. Zoabi and K. Margulis, *Mass Spectrom. Rev.*, 2023, **42**, 751-778.
34. M. Kompauer, S. Heiles and B. Spengler, *Nat. Methods*, 2017, **14**, 90-96.
35. M. Niehaus, J. Soltwisch, M. E. Belov and K. Dreisewerd, *Nat. Methods*, 2019, **16**, 925-931.
36. K. Ščupáková, B. Balluff, C. Tressler, T. Adelaja, R. M. Heeren, K. Glunde, and G. Ertaylan, *Clin. Chem. Lab. Med. (CCLM)*, 2020, **58**, 914-929.
37. E. Cortés, W. Xie, J. Cambiasso, A. S. Jermyn, R. Sundararaman, P. Narang, S. Schlu¨cker, and S. A. Maier, *Nat. Commun.*, 2017, **8**, 14880.
38. C. Zhan, J. Yi, S. Hu, X. G. Zhang, D. Y. Wu and Z. Q. Tian, *Nat. Rev. Methods Prime.,* 2023, **3**, 13.
39. A. Stefancu, N. J. Halas, P. Nordlander and E. Cortes, *Nat. Phy.,* 2024, **20**, 1065-1077.
40. A. Marimuthu, J. Zhang and S. Linic, *Science*, 2013, **339**, 1590-1593.
41. C. Clavero, *Nat. Photon.,* 2014, **8**, 95-103.
42. M. L. Brongersma, N. J. Halas and P. Nordlander, *Nat. Nanotech.*, 2015, **10**, 25-34.
43. J. A. Schuller, E. S. Barnard, W. Cai, Y. C. Jun and J. S. White, *Nat. Materials*, 2010, **9**, 193-204.
44. K. Wu, J. Chen, J. R. McBride and T. Lian, *Science*, 2015, **349**, 632-635.
45. A. J. Wilson and P. K. Jain, *Acc. Chem. Res.* 2020, **53**, 1773-1781.
46. S. Mubeen, J. Lee, N. Singh, S. Krämer, G. D. Stucky and M. Moskovits, *Nat.*

View Article Online
DOI: 10.1039/D5SC02632F

Nanotech. 2013, **8**, 247-251.

47. R. Chen, Z. Ren, Y. Liang, G. Zhang, T. Dittrich, R. Liu, Y. Liu, Y. Zhao, S. Pang, H. An, C. Ni, P. Zhou, K. Han, F. Fan and C. Li, *Nature,* 2022, **610**, 296-301.
48. C. D. Lindstrom and X. Y. Zhu, *Chem. Rev.*, 2006, **106**, 4281-4300.
49. S. W. Lee, *Tr. Chem.*, 2023, **5**, 561-571.
50. Y. Liu, Q. Chen, D. A. Cullen, Z. Xie and T. Lian, *Nano let.,* 2020, **20**, 4322-4329.
51. J. Repp, G. Meyer, F. E. Olsson and M. Persson, *Science*, 2004, **305**, 493-495.
52. J. Ji, A. E. Kline, A. Amoscato, A. K. Samhan-Arias, L. J. Sparvero, V. A. Tyurin, B. Fink, M. D. Manole, A. M. Puccio, D. O. Okonkwo, J. P. Cheng, H. Alexander, R. S. B. Clark, P. M. Kochanek, P. Wipf, V. E. Kagan and H. Bayır, *Nat. Neurosci.*, 2012, **15**, 1407-1413.
53. F. Fazio, L. Lionetto, G. Molinaro, H. O. Bertrand, F. Acher, R. T. Ngomba, S. Notartomaso, M. Curini, O. Rosati, P. Scarselli, R. D. Marco, G. Battaglia, V. Bruno, M. Simmaco, J. P. Pin, F. Nicoletti and C. Goudet, *Mol. Pharmacol.*, 2012, **81**, 643-656.
54. N. Y. Patil, H. Tang, L. Rus, K. Zhang and A. D. Joshi, *Mol. Pharmacol.,* 2022, **101**, 45-55.
55. M. Ulivieri, J. M. Wierońska, L. Lionetto, K. Martinello, P. Cieslik, A. Chocyk, M. Curto, L. D. Menna, L. Iacovelli, A. Traficante, F. Liberatore, G. Mascio, N. Antenucci, G. Giannino, M. Vergassola, A. Pittaluga, V. Bruno, G. Battaglia, S. Fucile, M. Simmaco, F. Nicoletti, A. Pilc and F. Fazio, *Schizophrenia Bull.*, 2020, **46**, 1471-1481.
56. L. Malinina, M. L. Malakhova, A. Teplov, R. E. Brown and D. J. Patel, *Nature*, 2004, **430**, 1048-1053.
57. T. T. Li, G. Li, R. Hu, X. Ji, C. Liu, Y. T. Shao, *Neurochem. Res.,* 2023, **48**, 2059-2065.
58. Q. Cao, X. Chen, X. Wu, R. Liao, P. Huang, Y. Tan, L. Wang, G. Ren, J. Huang, and C. Dong, *J. Exp. Med.* 2018, **215**, 1679-1692.
59. M. R. Bond and J. A. Hanover, *J. Cell Biol.,* 2015, **208**, 869-880.
60. R. A. Flynn, K. Pedram, S. A. Malaker, P. J. Batista, B. A. Smith, A. G. Johnson,

B. M. George, K. Majzoub, P. W. Villalta, J. E. Carette and C. R. Bertozzi, *Cell*, 2021, **184**, 3109-3124.

61. L. Wang, H. Qian, Y. Nian, Y. Han, Z. Ren, H. Zhang, L. Hu, B. V. V. Prasad, A. Laganowsky, N. Yan and M. Zhou, *Nature*, 2020, **581**, 329-332.
62. J. Remsik and A. Boire, *Nat. Rev. Cancer,2024,* **24**, 448–460.
63. A. E. Whiteley, D. Ma, L. Wang,S. Y. Yu, C. Yin, T. T. Price, B. G. Simon, K. R. Xu, K. A. Marsh, M. L. Brockman, T. M. Prioleau, K. L. Zhou, X. Cui, P. E. Fecci, W. R. Jeck, C. M. McCall, J. L. Neff and D. A. Sipkins, *Science*, 2024, **384**, eadh5548.
64. Z. Y. Yu, H. J. Li, M. Wang, W. Z. Luo and Y. K. Xue, *Int. J. Oncol.*, 2022, **61**, 1-2.
65. E. Guimaraes, R. Machado, M. D. Fonseca, A. Franca, C. Carvalho, A. C. Araujo e Silva, B. Almeida, P. Cassini, B. Hissa, L. Drumond and C. Goncalves, *PloS One*, 2017, **12**, e0175041.
66. A. Mound, A. Vautrin-Glabik, A. Foulon, B. Botia, F. Hague and J. B. Parys, *Oncotarget*, 2017, **8**, 72324.
67. Q. Sun, M. Li, G. Wang, H. Xu, Z. He, Y. Zhou, Y. Zhou, Y. Zhou, H. Song and H. Jiang, *Cancer Imaging*, 2019, **19**, 1-9.
68. E. J. Ge, A. L. Bush, A. Casini, P. A. Cobine, J. R. Cross, G. M. DeNicola, Q. P. Dou, K. J. Franz, V. M. Gohil, S. Gupta and S. G. Kaler, *Nat. Rev. Cancer*, 2022, **22**,102-113.
69. C. Wang, R. Zhang, X. Wei, M. Lv, Z. Jiang, *Adv. Immunol.*, 2020, **145**, 187-241.
70. Y. Shen, L. Howard and X. Y. Yu, *Materials*, 2024, **17**, 528.
71. K. S. Kulp, E. S. Berman, M. G. Knize, D. L. Shattuck, E. J. Nelson, L. Wu, J. L. Montgomery, J. S. Felton and K. J. Wu, *Anal. Chem.*, 2006, **78**, 3651-3658.
72. S. P. Fraser, J. K. Diss, A. M. Chioni, M. E. Mycielska, H. Pan, R. F. Yamaci, F. Pani, Z. Siwy, M. Krasowska, Z. Grzywna, W. J. Brackenbury, D. Theodorou, M. Koyutürk, H. Kaya, E. Battaloglu, M. T. De Bella, M. J. Slade, R. Tolhurst, C. Palmieri, J. Jiang, D. S. Latchman, R. C. Coombes and M. B. A. Djamgoz, *Clin.Cancer Res.*, 2005, **11**, 5381–5389.

73. S. H. Jang, K. S. Kang, P. D. Ryu and S. Y. Lee, *BMB Rep.*, 2009, 42, 535-539.

74. D. Lee and J. H. Hong, *Cancers*, 2021, **13**, 1473.

75. N. Kagara, N. Tanaka, S. Noguchi and T. Hirano, *Cancer Sci.*, 2007, **98**, 692-697.

Figure Legend

Figure 1. Hot electron transfer-driven ionization and the decay of gold plasmon. (A) plasmon induced hot-electron transfer (PHET). (B) direct metal-to-molecule interfacial charge transfer transition (DICTT) . (C) plasmon-induced metal-to-molecule interfacial charge transfer transition (PICTT) .

Figure 2. PICTT ionization and mass spectra of standard lipids on Au sputtered ITO glass slides. (A) Free fatty acids. (B) Phosphatidylglycerol.

Figure 3. PICTT ionization and mass spectrometric imaging on Au sputtered ITO slides. (A) Mass spectrometric imaging of Au^- ions alone. (B) Mass spectrometric imaging of Au^- ions with 9-AA auxiliary matrix. (C) Proton-coupled electron transfer to 9-AA and enhanced deprotonation of free fatty acids. (D) Comparison of PICTT MS and MALDI MS imaging of two tissue slices of a 4T1 tumor-bearing BALB/c nude mouse brain. O, X and Y are three adjacent brain slices from the mouse. Theoretical and experimental *m/z* values are labeled in the top or displayed in the bottom of pictures.

Figure 4. Mass spectrometric imaging of zwitterions in brain sections of 4T1 tumor-bearing BALB/c nude mouse with 9-AA auxiliary matrix. (A) Structures

View Article Online
DOI: 10.1039/D5SC02632F

of representative zwitterions. (B) PICTT MS imaging from Au sputtered ITO slide or non-Au sputtered ITO slide. X and Y are adjacent tissue slices.

Figure 5. PICTT two electron transfer ionization and mass spectrometric imaging of positive PC ions in brain sections of 4T1 tumor-bearing BALB/c nude mouse in negative ion mode with 9-AA auxiliary matrix. (A) Two electron transfer. (B) PICTT MS imaging on Au sputtered ITO slides or MS imaging by electron transfer on ITO slides without plasmonic Au nanoparticles. X and Y are adjacent tissue slices.

Figure 6. Comparison of PICTT and MALDI MS imaging of negative ions of brain sections of 4T1 tumor-bearing BALB/c nude mouse on Au sputtered ITO slides or non-Au sputtered ITO slides with 9-AA auxiliary matrix.

Figure 7. Spatial distribution of ions only detected in the brain of 4T1 tumor-bearing mouse. (A) Total 66 ions. (B) 9 phospholipids containing odd-numbered fatty acids. The order of averaged intensities of these ions is represented as red, yellow, blue and green, respectively.

Figure 8. PICTT MS imaging of metal ions and isotopes of a section M of 4T1 tumor-bearing BALB/c nude mouse on Au sputtered ITO slides with iohexol as auxiliary matrix.

View Article Online
DOI: 10.1039/D5SC02632F

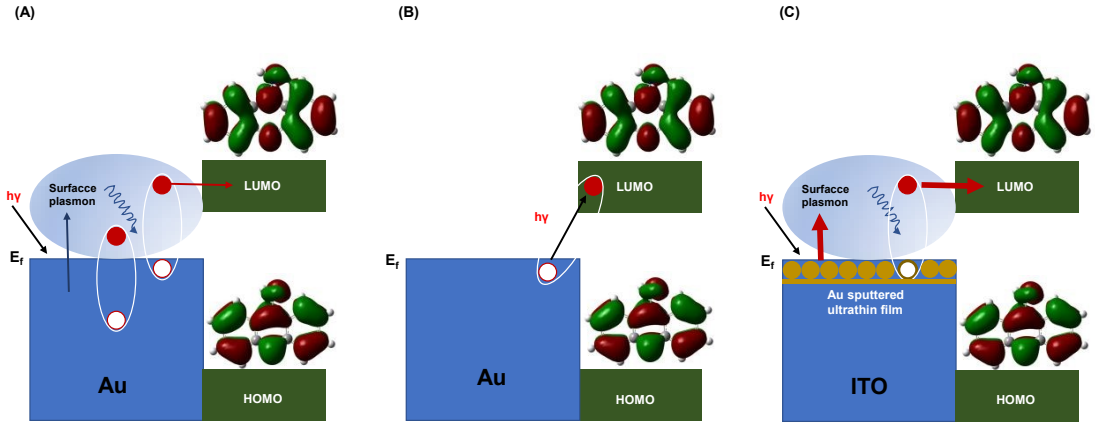

Figure 1

View Article Online
DOI: 10.1039/D5SC02632F

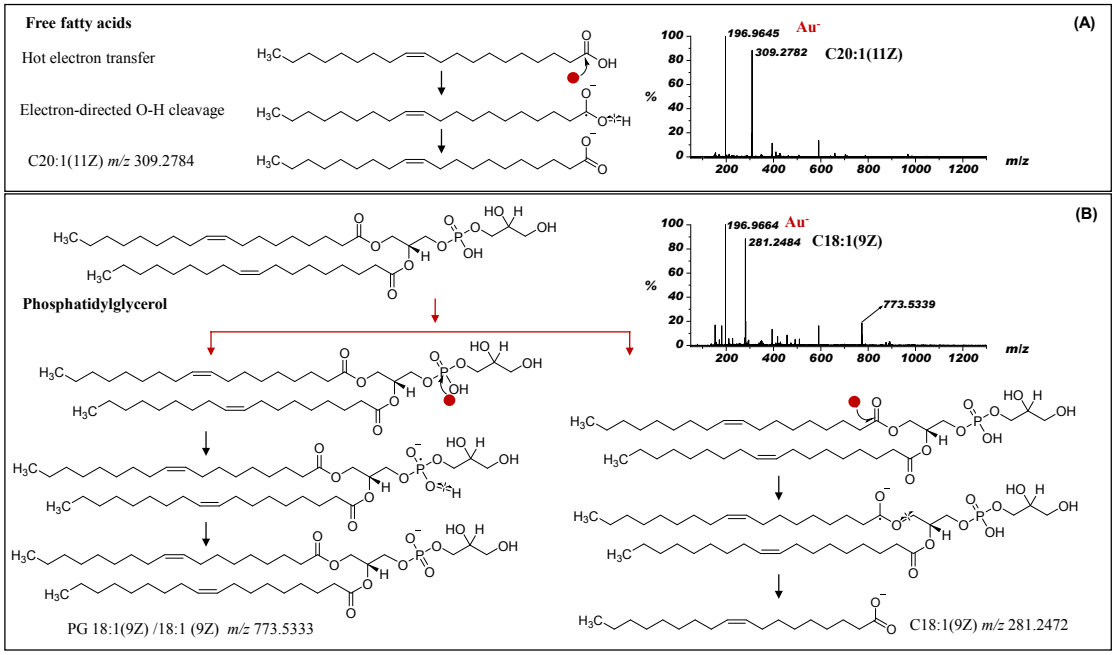

Figure 2

View Article Online
DOI: 10.1039/D5SC02632F

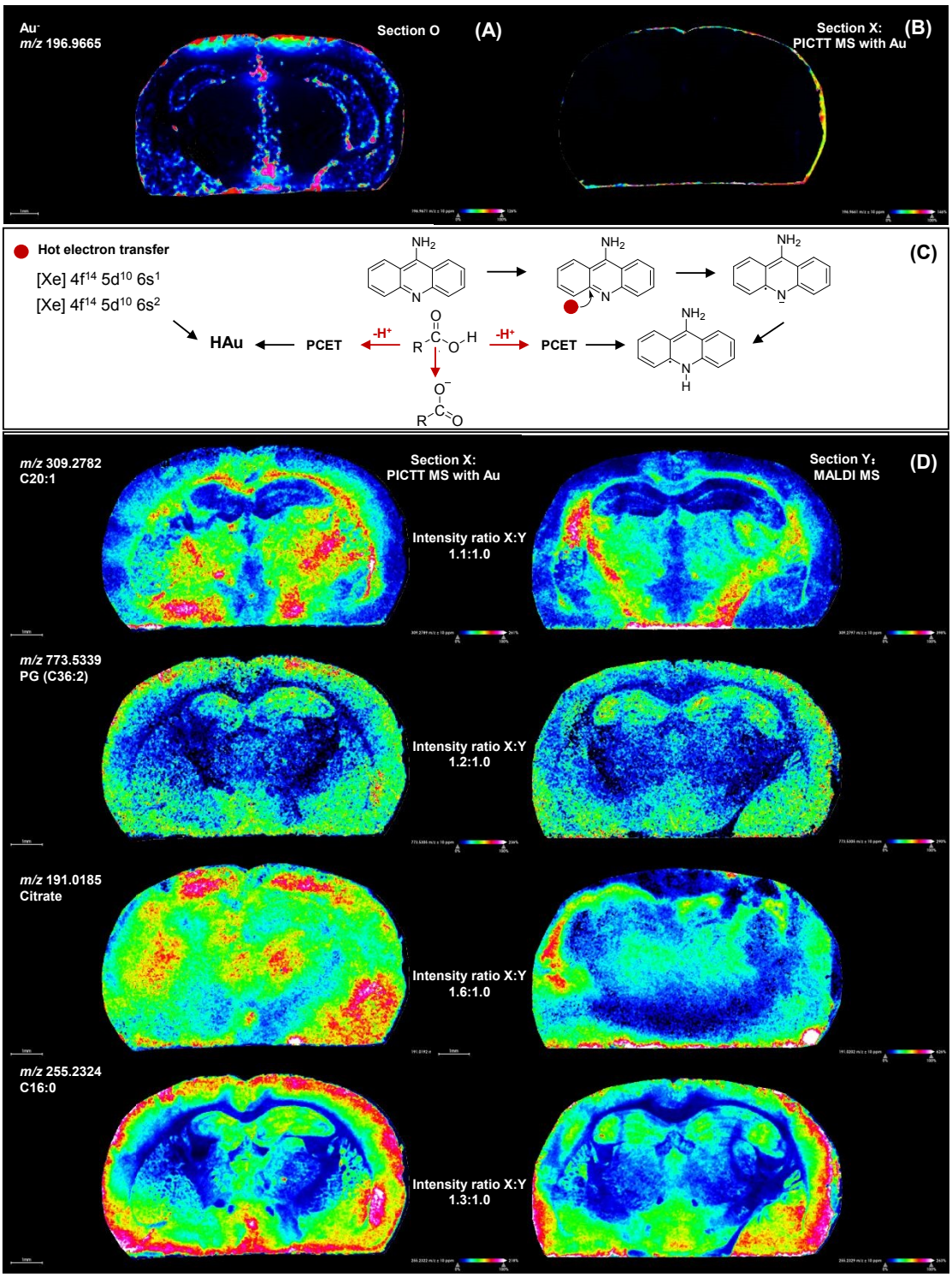

Figure 3

View Article Online
DOI: 10.1039/D5SC02632F

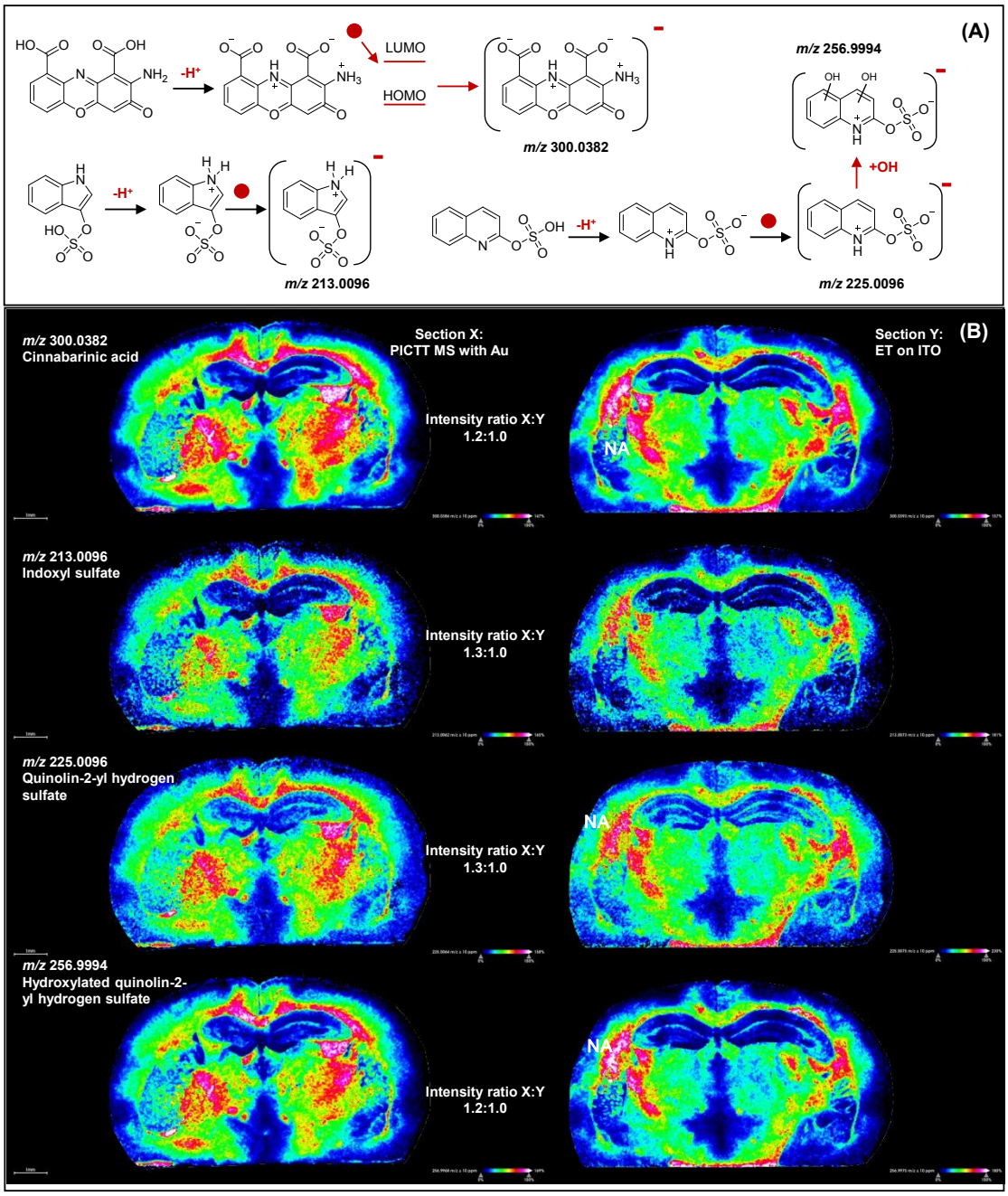

Figure 4

View Article Online
DOI: 10.1039/D5SC02632F

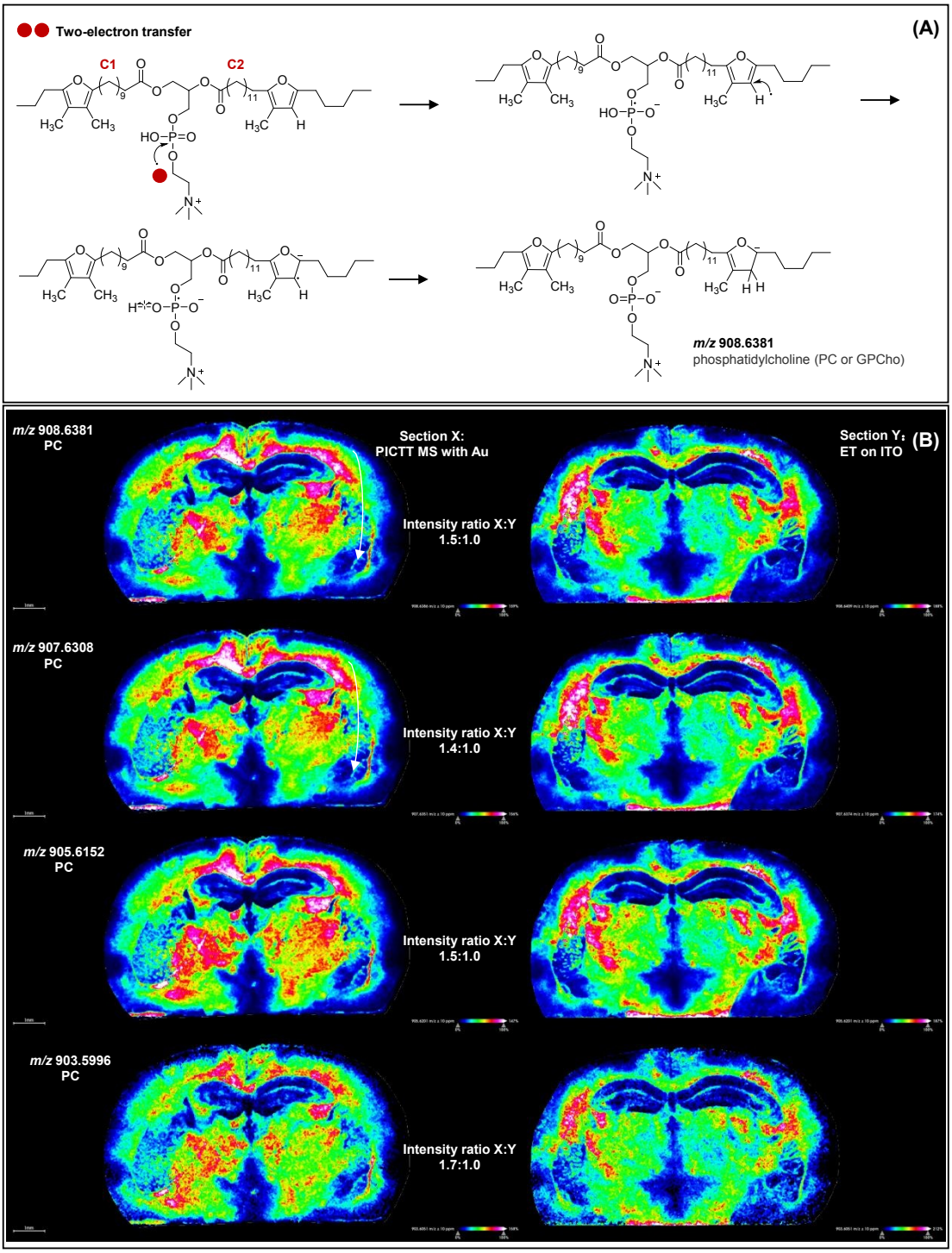

Figure 5

View Article Online
DOI: 10.1039/D5SC02632F

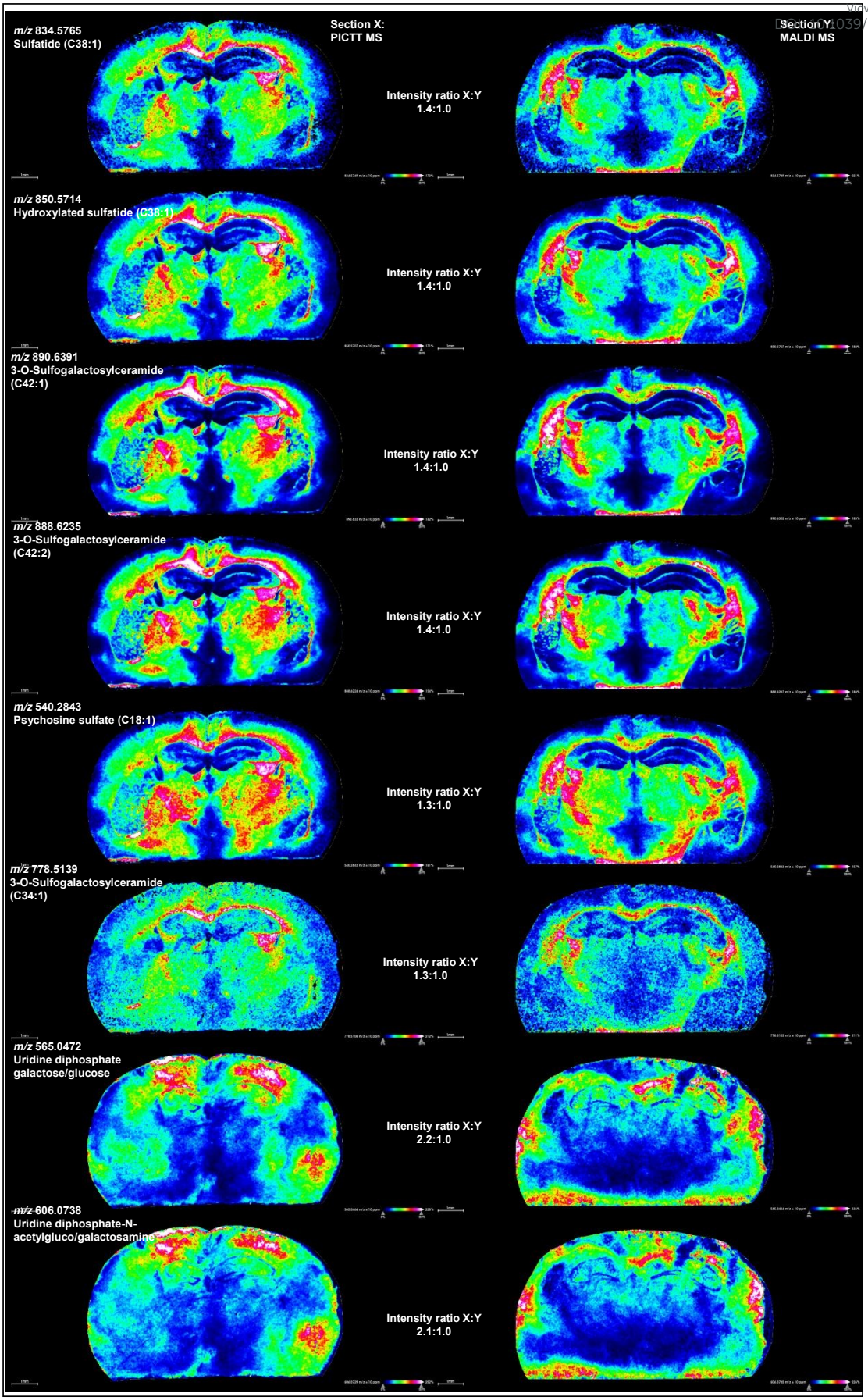

Figure 6

View Article Online
DOI: 10.1039/D5SC02632F

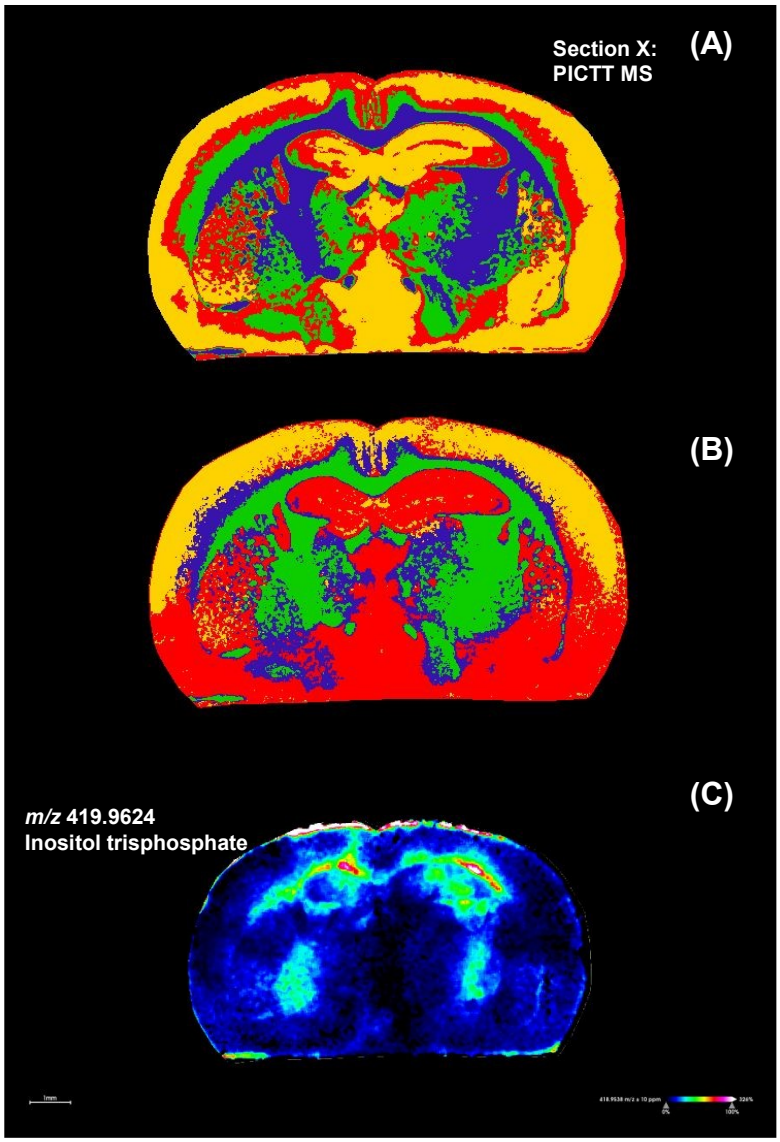

Figure 7

View Article Online
DOI: 10.1039/D5SC02632F

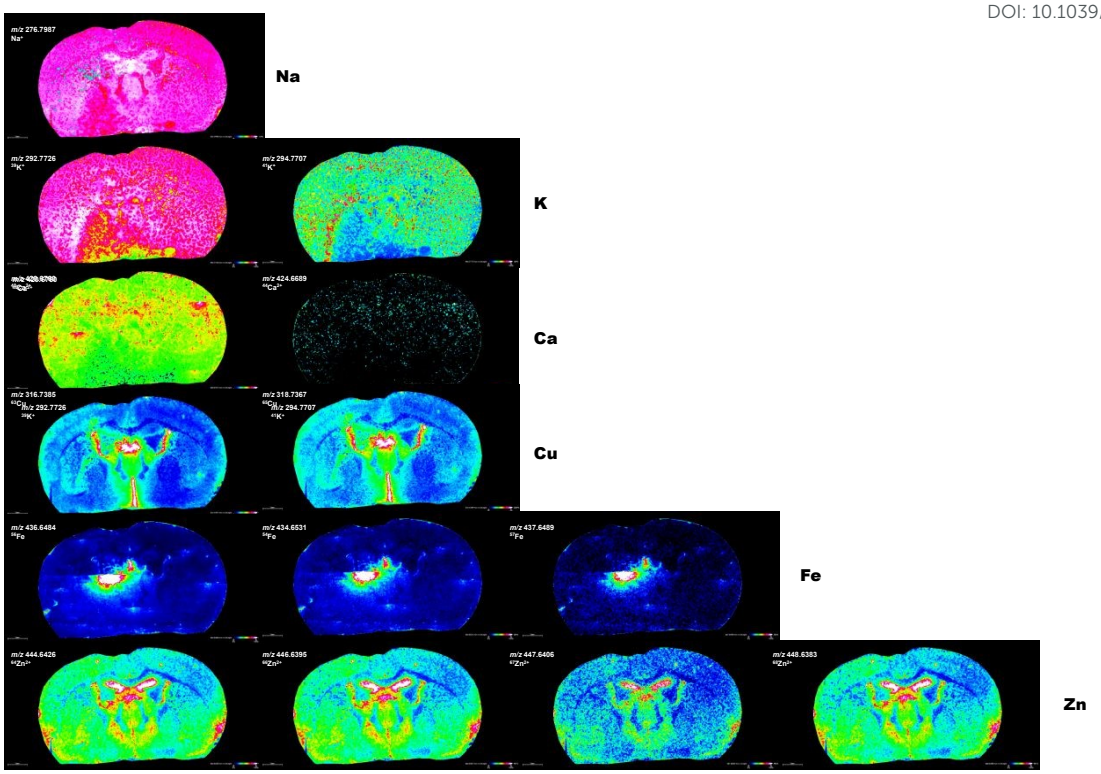

Figure 8

View Article Online
DOI: 10.1039/D5SC02632F

Data is available upon requested.